



RESEARCH ARTICLE

Optical properties of human brain and tumour tissue: An ex vivo study spanning the visible range to beyond the second near-infrared window

Jonathan Shapey^{1,2,3*}  | Yijing Xie³  | Elham Nabavi³ | Michael Ebner³ | Shakeel R. Saeed^{2,4,5} | Neil Kitchen² | Neil Dorward² | Joan Grieve² | Andrew W. McEvoy² | Anna Miserocchi² | Patrick Grover² | Robert Bradford² | Yau-Mun Lim⁶ | Sebastien Ourselin³ | Sebastian Brandner⁶ | Zane Jaunmuktane⁶ | Tom Vercauteren³

¹Wellcome/EPSCRC Centre for Interventional and Surgical Sciences, University College London, London, UK

²Department of Neurosurgery, National Hospital for Neurology and Neurosurgery, London, UK

³School of Biomedical Engineering & Imaging Sciences, King's College London, London, UK

⁴The Ear Institute, University College London, London, UK

⁵The Royal National Throat, Nose and Ear Hospital, London, UK

⁶Division of Neuropathology, UCL Queen Square Institute of Neurology, and The National Hospital for Neurology and Neurosurgery, University College Hospitals NHS Foundation Trust, London, UK

*Correspondence

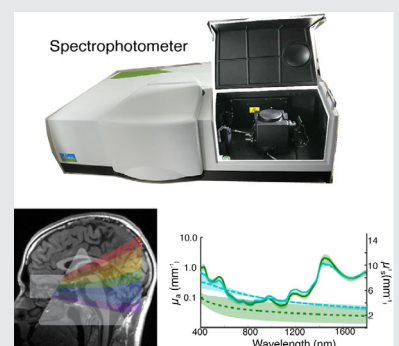
Jonathan Shapey, Wellcome/EPSCRC Centre for Interventional and Surgical Sciences, University College London, London
Email: jonathan.shapey@kcl.ac.uk

Funding information

Engineering and Physical Sciences Research Council, Grant/Award Numbers: NS/A000049/1, NS/A000050/1; National Brain Appeal, Grant/Award Number: NBA/T&I/N-ONC; Royal Academy of Engineering, Grant/Award Number: RCSR1819\7\34; Wellcome Trust, Grant/Award Numbers: 203145Z/16/Z, 203148/Z/16/Z, WT106882

Abstract

Neuro-oncology surgery would benefit from detailed intraoperative tissue characterization provided by noncontact, contrast-agent-free, noninvasive optical imaging methods. In-depth knowledge of target tissue optical properties across a wide-wavelength spectrum could inform the design of optical imaging and computational methods to enable robust tissue analysis during surgery. We adapted a dual-beam integrating sphere to analyse small tissue samples and investigated ex vivo optical properties of five types of human brain tumour (meningioma, pituitary adenoma, schwannoma, low- and high-grade glioma) and nine different types of healthy brain tissue across a wavelength spectrum of 400 to 1800 nm. Fresh and frozen tissue samples were analysed. All tissue types demonstrated similar absorption spectra, but the reduced scattering coefficients of tumours show visible differences in the



Jonathan Shapey and Yijing Xie have contributed equally to this study.

This is an open access article under the terms of the Creative Commons Attribution License, which permits use, distribution and reproduction in any medium, provided the original work is properly cited.

© 2022 The Authors. *Journal of Biophotonics* published by Wiley-VCH GmbH.

obtained optical spectrum compared to those of surrounding normal tissue. These results underline the potential of optical imaging technologies for intraoperative tissue characterization.

KEYWORDS

absorption, brain, brain tumour, optical properties, scattering, spectrophotometer

1 | INTRODUCTION

Optical imaging techniques are ideally suited for clinical use because they are noncontact, nonionising and noninvasive. They may be used for both diagnostic and therapeutic indications. Commonly used optical imaging modalities for diagnosis and surgical guidance include optical coherence tomography (OCT) [1–4] and fluorescence-based imaging techniques [5–7]. Emerging optical imaging techniques such as Raman spectroscopy [8–10], second generation harmonic (SGH) Imaging [11], diffuse reflectance spectroscopy [12], fluorescence lifetime imaging (FLIM) [13, 14], spatial frequency domain imaging (SFDI) [15, 16], photoacoustic (PA) imaging [17] and hyperspectral imaging (HSI) [18, 19] also have the potential to further transform the way surgery is performed by providing real-time tissue characterization and surgical guidance.

As light propagates across biological tissue, it undergoes multiple absorption and scattering events [20]. Optical characteristics of tissues are determined by the type of tissue and its constituents but may be altered by presence of disease and by surgery [21]. Tissue absorption is determined by a tissue's molecular composition and can serve as a spectral fingerprint for diagnostic purposes [22]. Tissue components absorbing light are called chromophores and may either be converted to heat or radiated in the form of luminescence (bioluminescence), including fluorescence and phosphorescence. Haemoglobin, lipid and water are the commonest biological chromophores in neural tissue although in cases of metastatic melanoma, melanin may also be an active chromophore in the brain [23]. Scattering is principally caused by the heterogenous subcellular composition of biological tissue but it also reflects a tissue's structural variation due to its extracellular membranous proteins. For tissue differentiation methods based on optical imaging techniques, an accurate understanding of the target tissue's optical properties can be critical in order to maximize their accuracy and efficacy. However, these optical properties are not yet fully known.

Neurosurgery, particularly neuro-oncology surgery, would especially benefit from detailed real-time intraoperative tissue characterization in order to improve the precision and efficacy of surgery. Protoporphyrin IX (PpIX) fluorescence-based imaging using 5-

aminolevulinic acid (5-ALA) is the current clinical standard for intraoperative real-time surgical guidance during glioma surgery [7]. However, visualization of malignant tissue boundaries using 5-ALA-PpIX fluorescence is unclear due to infiltration in healthy tissue, is nonquantitative due to the time-varying fluorescence effect, is associated with side effects and can only be used for specific tumour types. Several optical imaging methods are being investigated for various neuro-oncology applications but all presently developed systems are limited by their inability to deliver real-time intraoperative image analysis. This limitation may be alleviated by a-priori knowledge of optical tissue type properties.

Reliable determination of optical properties using integrating sphere reflectance and transmittance measurements is confounded by light escaped and lost out through the edges of samples due to finite sample size [24]. Consequently, the size of the available tissue sample has been a major limiting factor dictating the type of tissue that could be analysed in previous studies [25], meaning that only tissue from a limited number of larger tumours and large parenchymal brain regions have previously been characterized [26]. Furthermore, previous studies have only characterized the optical properties of brain tissue up to 1300 nm [25–27], whereas several optical imaging systems are capable of capturing spectral data beyond the second near-infrared window, typically up to 1800 nm [18].

In this study, we use of our adapted dual-beam integrating sphere system [28] to perform spectroscopic measurements of small biological, including human, tissue samples, enabling us to reliably measure the optical properties of small tissue samples measuring 4 to 7 mm in diameter. Building on our earlier preliminary results [29], this is the first study to investigate the optical properties of pituitary adenoma, vestibular schwannoma and parenchymal low-grade glioma, and healthy pituitary tissue, cranial nerves and dura. It is also the first study to provide data on the optical properties of human brain and tumour tissue (irrespective of neural tissue type) beyond 1300 nm, thus covering the second near-infrared window for biomedical imaging. Additionally, this is the first work to systematically examine whether there is a difference between the optical properties of fresh and

frozen human tissue samples and to correlate all samples with their corresponding histological appearance and nuclear density. To facilitate further work, the study's complete numerical dataset is released for use by the research community.

2 | METHODS

2.1 | Subjects

This study was approved by the NHS Health Research Authority (18/LO/1004). Patient tumour samples were obtained from the Brain Tumour Resource at the Department of Neuropathology, National Hospital for Neurology and Neurosurgery (NHNN). All samples came from adult patients who underwent surgery at the NHNN who consented to their tissue being stored and used in future research studies. Tissue samples were obtained from 17 different patients undergoing brain tumour surgery including four meningioma, six pituitary adenoma, four vestibular schwannoma, two high-grade glioma and one low-grade glioma. All tumour specimens were obtained fresh, processed within 20 min with optical measurements commenced within 30 min of resection.

Cadaveric healthy brain tissue was obtained from a single subject undergoing a post mortem examination at the Department of Neuropathology, NHNN, who had a valid consent form authorising the retention of tissue for ethically approved research purposes. Tissue samples from nine distinct anatomical regions including frontal grey matter, frontal white matter, anterior pituitary, pituitary stalk, pons, cranial nerve I, cranial nerve II, cranial nerve III, cranial nerve V and dura.

2.2 | Integrating sphere-based measurements

A dual-beam spectrophotometer (Lambda 750, Perkin Elmer, USA) with a 100 mm integrating sphere was adapted to measure the tissues' reflectance and transmittance spectra in the wavelength ranging from 400 to 1800 nm (Figures 1 and S1). The standard sample reflectance port dimensions are 17 mm × 22 mm and the transmittance port dimensions are 11 mm × 24 mm. We anticipated that a sample port size of 3 to 5 mm in diameter would be required to analyse the size of pathology specimens typically obtained at our institution. To meet these requirements, we adapted the integrating sphere using an adjustable light slit and a series of uncoated plano-concave lenses to collimate and focus the light appropriately thereby ensuring that the eventual beam size

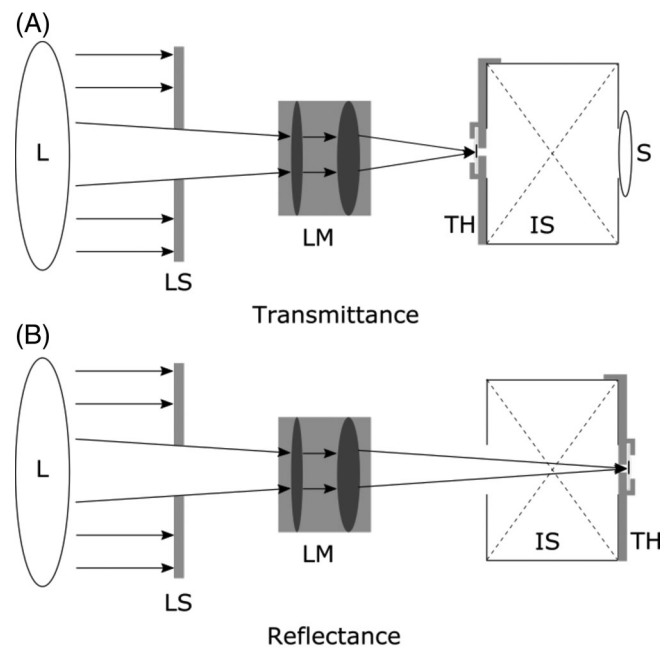


FIGURE 1 Schematic of experimental integrating sphere set up. IS, integrating sphere; L, lens module; LS, light source; LS, light slit; S, diffuse reflectance standard (Spectralon); TH, tissue holder; Shaded areas represent additional components. (A) Transmittance lens module comprised -150 and $+60$ lens. PMT settings: Gain: Auto, Response time: 0.8 s, InGaAs settings: Gain: 5, Response time 0.8 s. 3 mm set up: Slit width: 5 mm; Resulting beam size at the port: 1×1.5 mm. 5 mm set up: Slit width: No slit; Resulting beam size at the port: 2×2 mm. (B) Reflectance lens module comprised -150 and $+200$ lens. PMT settings: Gain: Auto, Response time: 0.8 s, InGaAs settings: Gain: 12, Response time 0.8 s. 3 mm set up: Slit width: 3 mm; Resulting beam size at the port: 2×2 mm. 5 mm set up: Slit width: 5 mm; Resulting beam size at the port: 2×3.5 mm

was smaller than the anticipated sample size. Bespoke adapters with small-sized sample ports to hold the tissue slides were 3D printed and tissue slides were manually manufactured using 2 mm thick acrylic. The internal side facing the integrating sphere consisted of a patch of PTFE (Zenith Lite, Pro Lite, Cranfield, UK) that covered the original port of the integrating sphere and matched its internal material. The experimental setup was validated with a standard tissue-mimicking optical phantom previously characterized with the same machine using standard sample reflectance and transmittance ports [28].

2.3 | Sample preparation and analysis

All specimens were processed according to the study protocol. For each tumour specimen, four samples were obtained; two for fresh analysis and two for analysis after freezing. The maximum sized tissue was selected, and the

specimen was placed in the chamber of a suitably sized slide ensuring that the tissue completely covered the central 3 or 5 mm hatched area. All specimens were cut by hand to thickness of approximately 2 mm. Index matching gel (Thorlabs, Cat no: G608N3) was used to secure the tissue in place by filling the empty region within the chamber at either end of the specimen. Two specimens were immediately snap frozen using Frosbite rapid coolant spray (Leica Microsystems [UK] Ltd). A small amount of Pertex mounting medium was applied to the sides of the specimen chamber and a coverslip was placed on top of the specimen to seal the specimen within the central chamber. Frozen specimens were stored at -80°C and analysed at least 7 days later, once thawed at room temperature for at least 30 min. Three reflectance and transmittance measurements were obtained for each of the four samples.

In total, 174 paired total reflectance and total transmittance measurements (R_T , T_T) were performed (138 tumour measurements and 36 cadaveric measurements). Once all optical measurements had been completed, the tissue was returned to the Department of Neuropathology on the same day and the specimens were placed in formalin, stained with haematoxylin and eosin (H&E) and prepared for histopathological analysis. A formal diagnosis was provided for each tissue specimen, including a comment on the sample's cellular morphology and microstructure. Using open-source QuPath software (QuPath v.0.2.0-m5, Quantitative Pathology & Bioimage Analysis, University of Edinburgh) [30], the number of nonneuronal nuclei per sample were calculated, providing a quantifiable metric of cellular density (nuclei per mm^2).

2.4 | Data processing

An inverse adding-doubling (IAD) method developed by Prahl et al. [31] as used to calculate the tissue's intrinsic optical properties, absorption μ_a and reduced scattering μ'_s , from the integrating sphere measurement of the total reflectance (R_T) and total transmission (T_T) spectra for each sample [31]. The IAD is a reverse procedure of the numerical approach to the one-dimensional radiation transport equation (RTE). The implementation of IAD by Prahl et al. includes anisotropic scattering and internal reflection at the sample boundaries, and validated corrections for measurements made with integrating spheres [31]. Thus, it is a preferable method for determining optical properties of excised biological samples that are mounted between two glass slides in combination of integrating sphere measurements, with an acceptable trade-off between accuracy and computation speed.

The input parameters of the IAD were defined according to the integrating sphere measurement setups, and a fixed

index of refraction of brain tissues was predetermined to be 1.40 for all brain tissue types [25]. Since only two integrating sphere measurements (R_T and T_T) were obtained in this study, a fixed anisotropy coefficient $g = 0.85$ was used in the calculation for every wavelength and sample types, similar to previous studies [25, 27]. Absorption and reduced scattering coefficients were computed for each specimen and used to calculate mean and SD values for each tissue type. Data points that did not converge for individual wavelengths using our specified constraints were excluded when calculating the wavelength-wise mean values. A total of 24 534 wavelength measurements were obtained in the study (174 samples \times 141 measured wavelengths); 2437 (9.9%) individual single-wavelength measurements were excluded because convergence criteria of the IAD algorithm were not met and were thus considered unreliable. No samples were completely excluded.

Albedos between 0.4 and 0.95 are considered intermediate values [24] and the IAD method is considered to be ideally suited for such samples ($A = \mu'_s[\mu_a + \mu'_s]^{-1}$). However, it has been acknowledged that inter-parameter crosstalk effects exist at wavelengths where the absorption is much higher than the scattering, for example, at the high haemoglobin and water absorption wavelengths. At these wavelengths, the resulting low albedo value creates nonconformity peaks in the IAD-calculated reduced scattering spectra and fails to conform to typical Mie scattering theory whereby scattering monotonically decreases with wavelength [25]. To mitigate the crosstalk artefact in reduced scattering estimations, further model fitting using equation (Equation 1) was applied to the IAD-calculated reduced scattering.

$$\mu'_s(\lambda) = \mu'_s{}^{500} \left(f_{\text{Ray}} \left(\frac{\lambda}{\lambda_{\text{ref}}} \right)^{-4} + (1 - f_{\text{Ray}}) \left(\frac{\lambda}{\lambda_{\text{ref}}} \right)^{-b_{\text{Mie}}} \right) \quad (1)$$

The Rayleigh scattering is expressed as $a f_{\text{Ray}} (\lambda/\lambda_{\text{ref}})^{-4}$, and the Mie scattering is denoted as $a (1 - f_{\text{Ray}}) (\lambda/\lambda_{\text{ref}})^{-b_{\text{Mie}}}$, where $a = \mu'_s{}^{500}$, f_{Ray} and $1 - f_{\text{Ray}}$ indicate the fraction of Rayleigh scattering and Mie scattering, respectively. The power factor 4 for Rayleigh scattering was determined in previous studies, whilst b_{Mie} is the "scattering power" of Mie scattering¹⁵. A second equation (Equation 2) in which the Mie scattering is not separated into Rayleigh and Mie scattering fractions is used to compare with Equation (1). The three considerations for using additional Equation (2) fitting are: (1) to compare scattering power b with b_{Mie} in Equation (1) for analysing whether Rayleigh scattering has an effect; (2) to compare the $\mu'_s{}^{500}$ and b with values from other reports; (3) to use as constrain input for IAD to generate revised μ_a to

mitigate the crosstalk effect. In both equations, wavelength λ is normalized by a reference wavelength, $\lambda_{\text{ref}} = 500$ nm, to yield a dimensionless value; and a scaling factor $\mu'_s{}^{500}$ is applied. The reference wavelength and scaling factor were chosen to enable us to directly compare our results with the findings of Jacques [23] where a simpler mathematical model was employed.

$$\mu'_s(\lambda) = \mu'_s{}^{500} \left(\frac{\lambda}{\lambda_{\text{ref}}} \right)^{-b} \quad (2)$$

For both models, we used nonlinear least square fitting to find the fitting parameters to the IAD calculated μ'_s datasets. In order to avoid the aforementioned crosstalk affected regions, we applied the fittings to μ'_s spectra for $\lambda \in [450, 1300]$ nm to determine f_{Ray} , b_{Mie} and b using Equation (1). In some biological tissues, cellular structures are the dominate scattering particles that interact with the incident light. In these cases, the wavelength-dependent reduced scattering presents a simple power law that can be described with Equation (2), and the “scattering power” b is related to the mean size of the cellular structures which can potentially be used to characterize tissue type [23, 32, 33]. However, in some collagenous and fibrous tissues, the Rayleigh scattering is more evident than in other tissues, speculatively due to their sub-micron collagen structures. Hence, the f_{Ray} and b_{Mie} in Equation (1) could be indicative of the effect of these sub-micron structures [23, 32, 33].

Gebhart et al. reported that the inter-parameter crosstalk effect between the IAD calculated μ_a and μ'_s might be caused by nonlinearities in the integrating sphere measurements of low reflectance levels. In order to mitigate the crosstalk effect on μ_a , we utilized a two-stage IAD workflow and validated it by Monte Carlo (MC) simulation on computational simulated phantoms (Table S1). A pair of primary μ_a^{IAD} and μ'_s were calculated from the input pair of reflectance and transmittance spectra (R_T , T_T) by the first layer of IAD. Then, the μ'_s which was affected by crosstalk was fitted by power law according to Mie theory Equation (2), as in the previous section. The fitted $\mu'_s{}^{\text{fit}}$ together with the original measurements of R_T and T_T were used as inputs for the second layer of IAD to calculate a revised absorption coefficient μ_a^{rev} .

3 | RESULTS

3.1 | Integrating sphere measurements

The mean value of measured total reflectance spectra R (R_T) and total transmittance spectra T (T_T) of each

tumour tissue type are presented in Figure 2. Results are plotted alongside the optical properties of tissues commonly encountered during surgery for that particular tumour. Higher scattering gives higher R value, and the shape of the R spectra is affected by the tissue's absorption, with absorption peaks corresponding to dips in the R spectra. The absorption peaks of oxygenated haemoglobin (HbO_2) at 415, 535 and 575 nm and deoxygenated haemoglobin (Hb) at 435 and 560 nm are prominent in all tissue types. Dips in R spectra at 975, 1200, and 1450 nm are noticeable in all tissue types and align with the water absorption peaks. Lipid absorption peaks at 1210 nm are most pronounced in pons, cranial nerves and white matter, suggesting a relative high lipid concentration in these tissues with additional lipid absorption peaks at 1720 and 1760 nm also observed in pons and white matter. In contrast to R , the transmittance spectra T decrease with increased scattering. However, similar to R , the spectral shape of T is dominated by absorption spectra, with dips corresponding to haemoglobin (Hb , HbO_2), water and lipid absorption, respectively. Figure S2 provides mean and SD values of total reflectance (R_T) and total transmittance (T_T) of meningioma, pituitary adenoma and schwannoma, and a comparison between fresh and frozen samples is also illustrated in this figure.

3.2 | Optical properties of brain and tumour tissue

Figures 3–6 illustrate the revised mean absorption (μ_a^{rev}) and reduced scattering ($\mu'_s{}^{\text{fit}}$) coefficient spectra of meningioma (Figure 3), pituitary adenoma (Figure 4), schwannoma (Figure 5) and glioma (Figure 6). Comparative results for fresh and frozen samples are provided for meningioma, pituitary adenoma and schwannoma (Figures 3–5). As detailed in the methods section, the revised absorption (μ_a^{rev}) spectra was calculated with $\mu'_s{}^{\text{fit}}$ as an input constraint of the two-stage IAD process that addressed crosstalk between absorption and scattering spectra.

Table S1 includes the revised mean absorption (μ_a^{rev}) reduced scattering and model-fitted $\mu'_s{}^{\text{fit}}$ values for each tissue type in 10 nm increments within the measured wavelength spectra of 400 to 1800 nm with corresponding values from the literature provided for comparison. All tumour types shared qualitatively similar dependencies of the optical properties on the wavelength (Figures 3–6). The absorption spectra of all samples had a series of peaks below 600 nm and above 900 nm, typically associated with the absorption bands of haemoglobin and water, respectively [34]. Low absorption values were

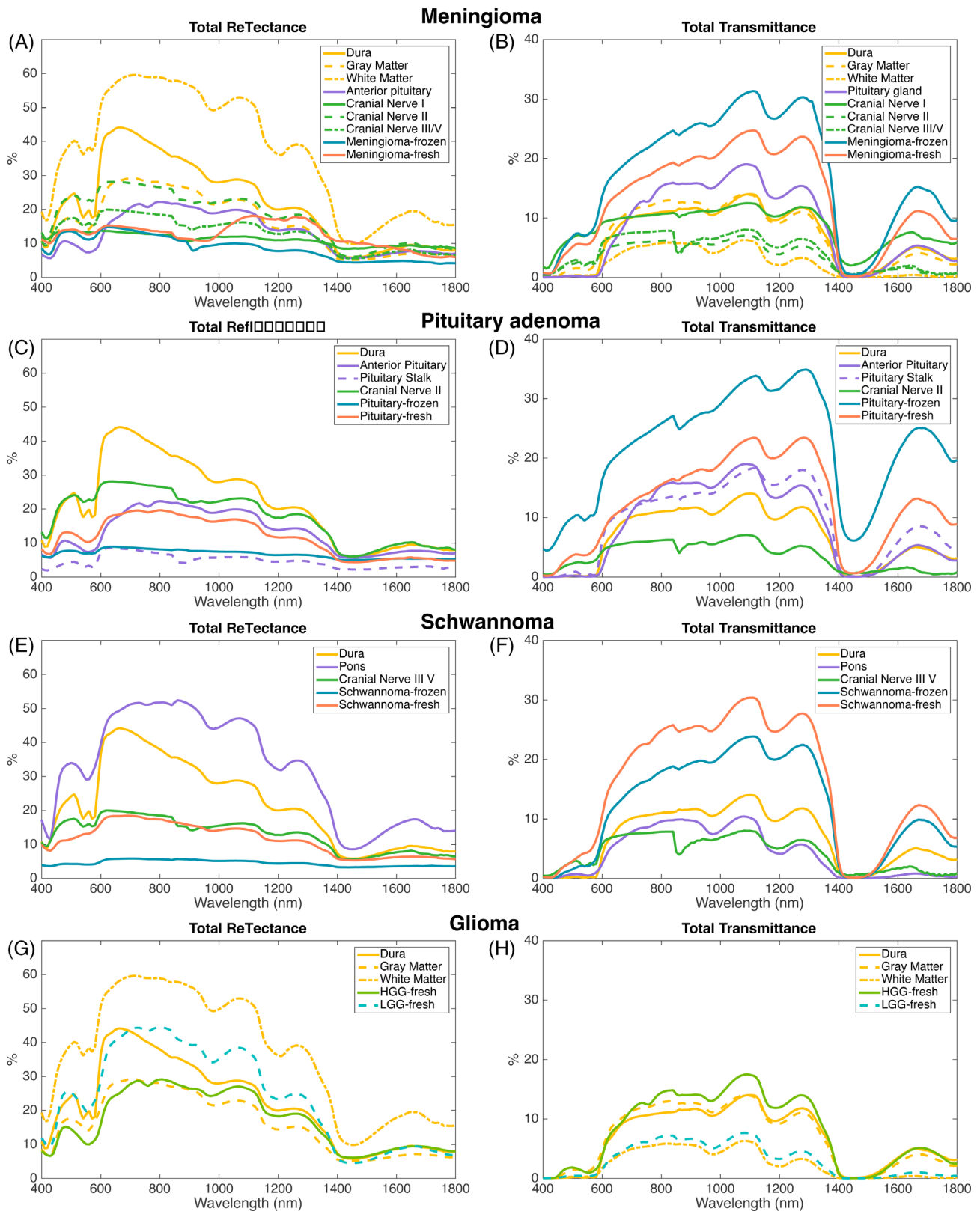


FIGURE 2 Total reflectance and total transmittance spectra of brain tumour and associated healthy brain tissues. Results are plotted alongside the optical properties of tissues commonly encountered during surgery for that particular tumour. (A, B) Meningioma plotted alongside dura, grey matter, white matter, anterior pituitary, cranial nerve I, II, and III/V; (C, D) Pituitary adenoma plotted alongside dura, grey matter, white matter, anterior pituitary, pituitary stalk and cranial nerve II; (E, F) Schwannoma plotted alongside dura, pons and cranial nerve III/V and (G, H) Glioma (including low- and high-grade glioma) plotted alongside dura, grey matter and white matter

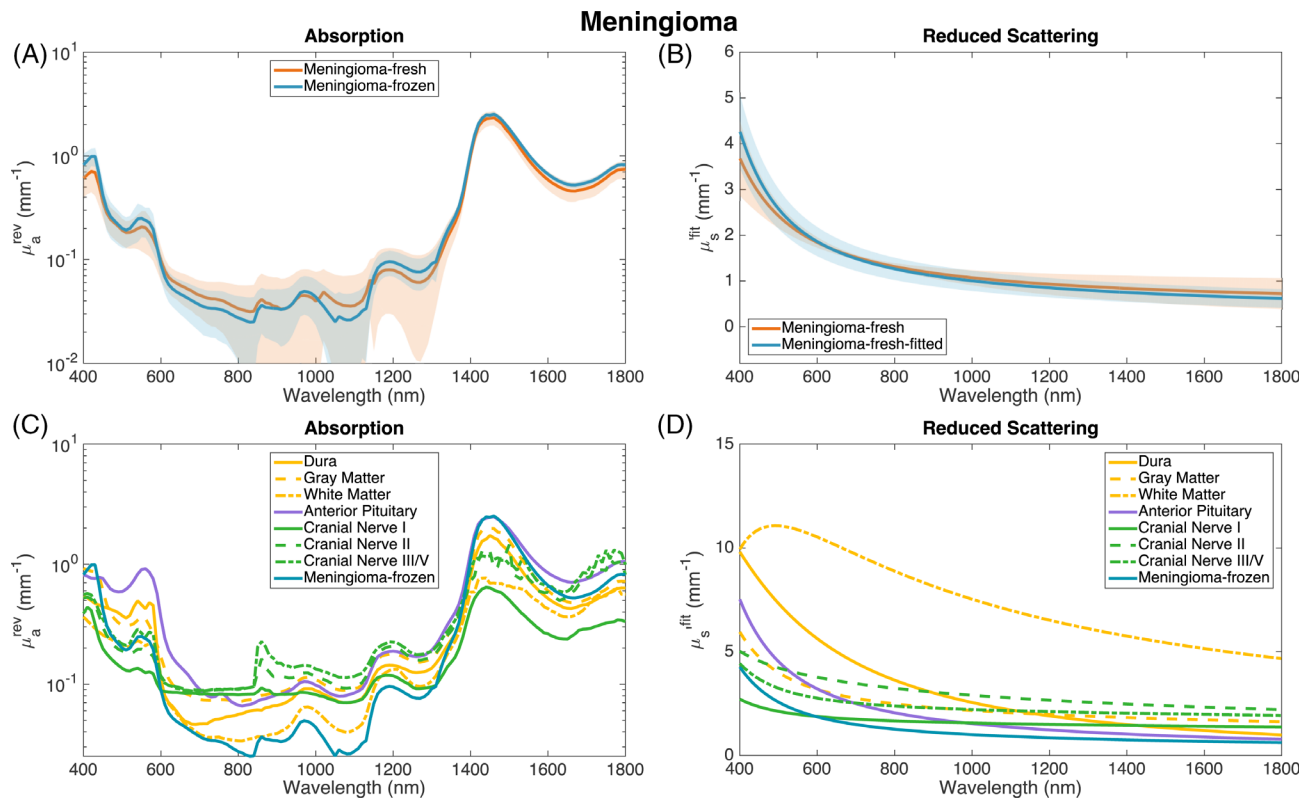


FIGURE 3 Absorption and reduced scattering coefficient of meningioma. (A, B) Mean and SD of (A) revised absorption (μ_a^{rev}) and (B) model-fitted reduced scattering coefficient (μ_s^{fit}) for fresh and frozen meningioma samples. (C, D) Mean μ_a^{rev} (C) and mean μ_s^{fit} (D) for frozen meningioma and related cadaveric tissues (dura, grey matter, white matter, anterior pituitary and cranial nerves I, II and III/V). μ_a^{rev} of all tissues are dominated by the absorption bands of haemoglobin (below 600 nm) and water (above 900 nm; A and C). μ_s^{fit} generally decreased with increasing wavelength (B and D)

observed within the 600 to 900 nm wavelength range. The absorption spectra of all five tumour types also demonstrated peak absorption bands around 430 and 550 nm characteristic of oxy- and deoxy-haemoglobin, respectively (Figures 3–6) [35].

Reflectance measurements are characterized by haemoglobin and lipid peaks with dips corresponding to water absorption peaks. Transmittance measurements are also dominated by absorption spectra with dips corresponding to haemoglobin, water and lipid absorption.

The reduced scattering coefficient of all tumours generally decreased with increasing wavelength, consistent with the Rayleigh limit of Mie scattering (Equation 1). All tumour spectra contained two modest scattering peaks at 430 and 550 nm consistent with the corresponding haemoglobin absorption spectra but, most strikingly, all five tumour types also exhibited a very prominent peak in μ_a^{rev} at 1450 nm, corresponding to a similarly pronounced water-related absorption peak at the same wavelength. Values for the model-fitted μ_s^{fit} spectra demonstrated a curve that conformed well to the expected trend (as detailed below) and provided a robust method to compare relative spectra (Figures 3–6).

Tumours could be differentiated from associated normal tissue by the strength and shape of their μ_s^{fit} values. In particular, low-grade glioma (LGG) demonstrated consistently higher μ_s^{fit} mean values compared to other tumour tissue at any given wavelength and its reduced scattering spectra were distinguishable from those of high-grade glioma (HGG). Some of the calculated reduced scattering spectra demonstrated high variability, especially that of fresh pituitary tumour tissue (Figure 4). Within the wavelength range of 700 to 1100 nm, the differentiating water peaks seen in the absorption spectra of fresh tumour tissue appeared less pronounced in the frozen samples and generally returned higher μ_a^{rev} values. Absorption spectra above 1200 nm appeared largely similar. These results suggest that the freezing process does affect the absorption and reduced scattering spectra of neural tissues, particularly within the 700 to 1100 nm wavelength range.

Healthy cadaveric brain tissue (Figures 3–6) displayed similar absorption peaks related to the presence of haemoglobin and water in addition to the expected low absorption values within the wavelength range of 600 to 900 nm. The reduced scattering spectra of healthy brain tissue also demonstrated typical decreasing values with

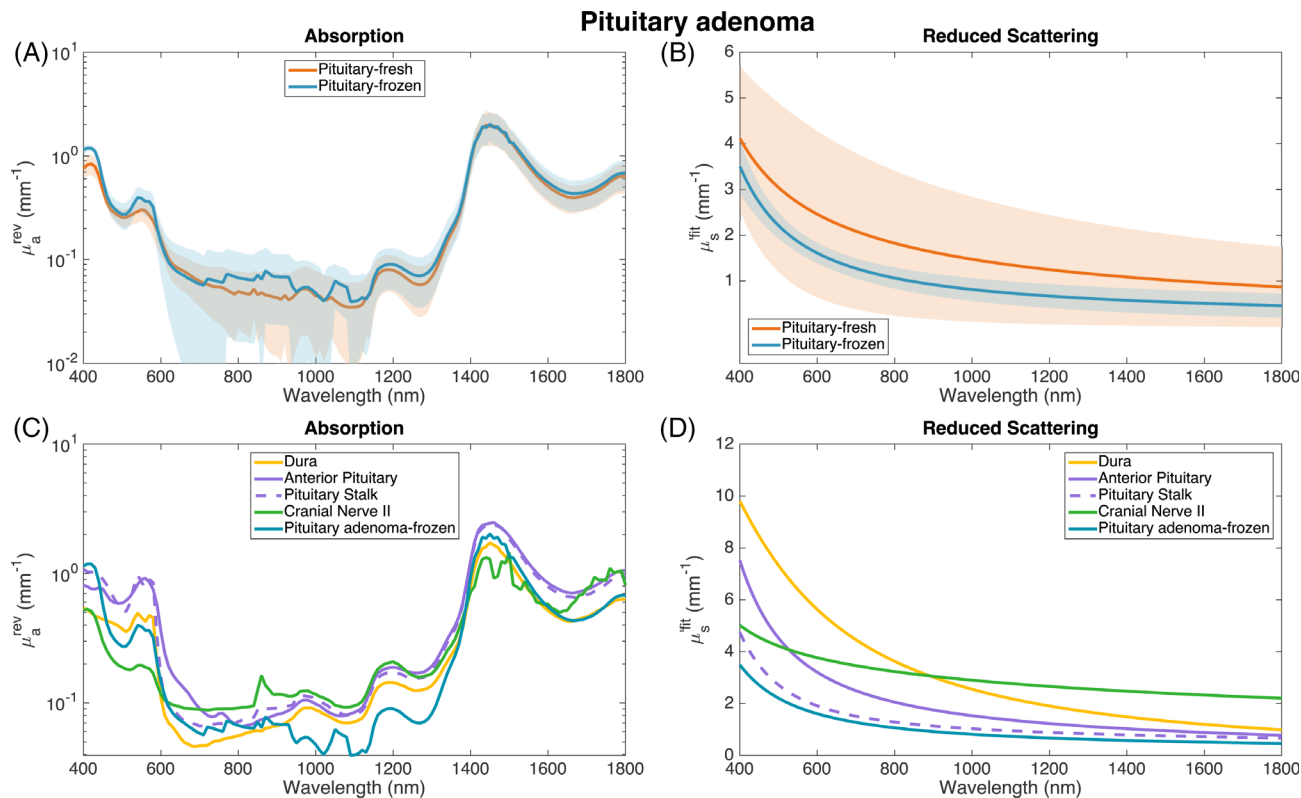


FIGURE 4 Absorption and reduced scattering coefficient of pituitary adenoma. (A, B) Mean and SD of (A) revised absorption (μ_a^{rev}) and (B) model-fitted reduced scattering coefficient (μ_s^{fit}) for fresh and frozen pituitary adenoma samples. (C, D): Mean μ_a^{rev} (C) and mean μ_s^{fit} for frozen pituitary adenoma and related cadaveric tissues (dura, anterior pituitary, pituitary stalk and cranial nerves II). μ_a^{rev} of all tissues are dominated by the absorption bands of haemoglobin (below 600 nm) and water (above 900 nm; A and C). μ_s^{fit} generally decreased with increasing wavelength (B and D)

increasing wavelength and could be differentiated by their respective reduced scattering spectra (Figures 3–6). The relative levels of reduced scattering were highest for white matter at all investigated wavelengths. However, the peak at 1450 nm seen in other brain tissue types was far less marked in white matter. Pons tissue demonstrated a spectral curve between that of grey and white matter and the reduced scattering spectra of cranial nerves was lower than that of parenchymal brain tissue.

3.3 | Histological analysis and measurement of cellularity

Each tissue sample was categorized by its morphological appearance and the specimen's nuclear density was calculated from a digital image using the digital image analysis software QuPath (Table 1) [30]. Tumour tissue had a higher nuclear density than normal tissue (Table 1 and Figure 7). Pituitary adenoma had the highest nuclear density of the reported tumour types with a mean nuclear density of approximately 8100 nuclei/ mm^2 , followed by meningioma (~ 5200 nuclei/ mm^2), schwannoma (3900

nuclei/ mm^2) and glioma. HGG had a higher nuclear density compared to LGG (~ 3700 and ~ 800 nuclei/ mm^2 , respectively), with the nuclear density of LGG below that of normal white matter (~ 1500 nuclei/ mm^2). The nuclear density of tissue did not appear to be altered by the freezing process (Figure 7).

3.4 | Correlation of optical scattering coefficients and tissue morphology

The optical scattering property of tissue offers information on the size, and concentration of the effective scattering particles within the tissue. Figure 7A illustrates the correlation between the ratio of b_{Mie}/b and f_{Ray} and, as expected, the fraction of b_{Mie}/b decreases when the Rayleigh scattering became predominate (an increase in f_{Ray}). Furthermore, Figures 7B–D appear to demonstrate the absence of a strong correlation between the nuclei density and the features of scattering (scattering power b , scattering power b_{Mie} , and μ_s 500). Presumably, the mean size of the contributing scatters is not significantly reflected by the tissue's nuclei density.

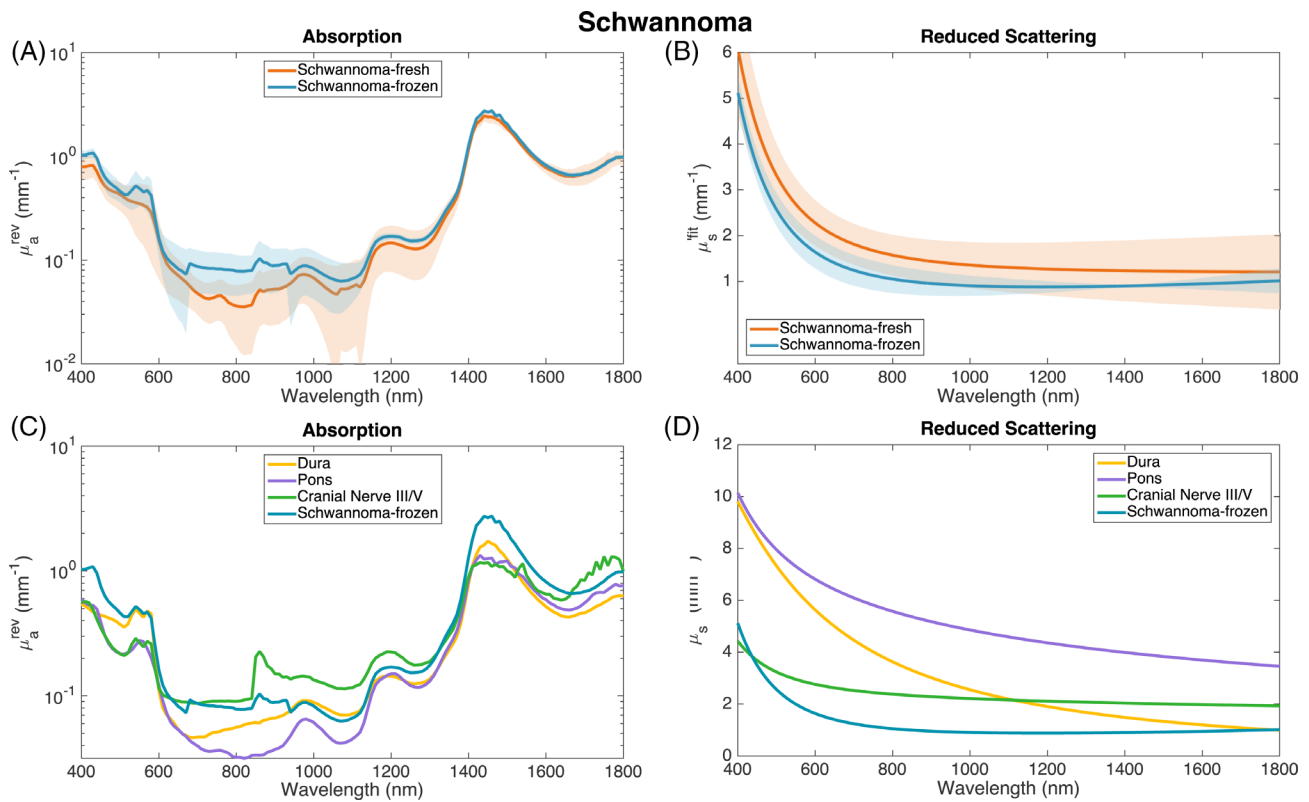


FIGURE 5 Absorption and reduced scattering coefficient of schwannoma. (A, B) Mean and SD of (A) revised absorption (μ_a^{rev}) and (B) model-fitted reduced scattering coefficient (μ_s^{fit}) for fresh and frozen schwannoma samples. (C, D) Mean μ_a^{rev} (C) and mean μ_s^{fit} for frozen schwannoma and related cadaveric tissues (dura, pons, and cranial nerves III/IV). μ_a^{rev} of all tissues are dominated by the absorption bands of haemoglobin (below 600 nm) and water (above 900 nm; A and C). μ_s^{fit} generally decreased with increasing wavelength (B and D)

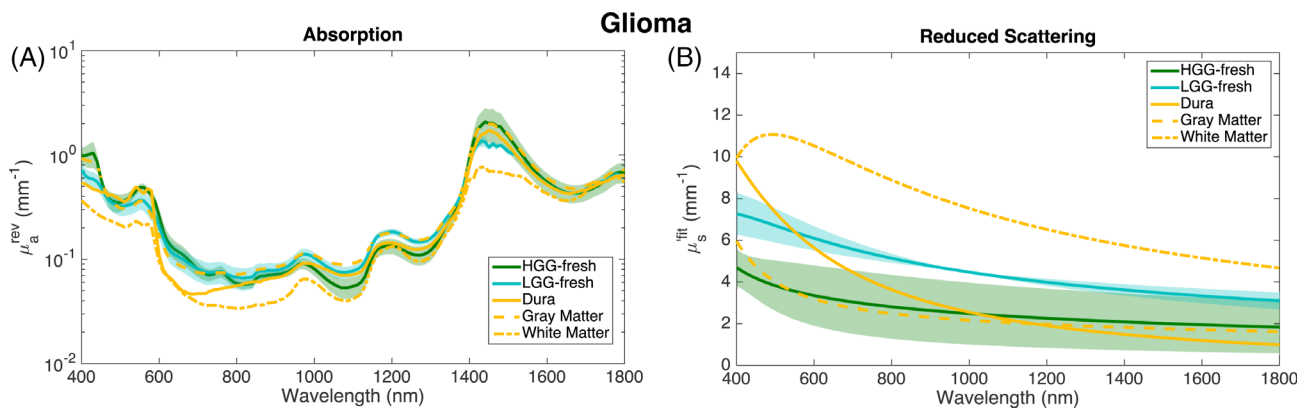


FIGURE 6 Absorption and reduced scattering coefficient of low- and high-grade glioma. (A, B): Mean and SD of (A) revised absorption (μ_a^{rev}) and (B) model-fitted reduced scattering coefficient (μ_s^{fit}) for fresh glioma and related cadaveric tissues (dura, grey matter and white matter). Absorption spectra of all tissues are dominated by the absorption bands of haemoglobin (below 600 nm) and water (above 900 nm; A). μ_s^{fit} generally decreased with increasing wavelength (B)

4 | DISCUSSION

Optical imaging methods have the potential to transform neurosurgery by providing a means for intraoperative tissue differentiation. In-depth knowledge of target tissue optical properties across the wide-wavelength spectra can

help inform the design of optical imaging and computational methods therefore enabling robust and interpretable tissue analysis which is critical for surgery. In this study, we investigated the ex vivo optical properties of five types of human brain tumour and nine different types of healthy brain tissue across a wavelength

TABLE 1 Representative histology and nuclear density of brain and tumour tissue

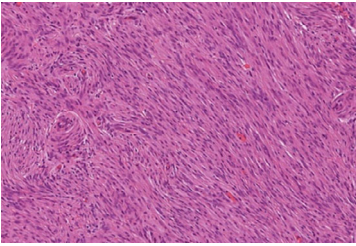
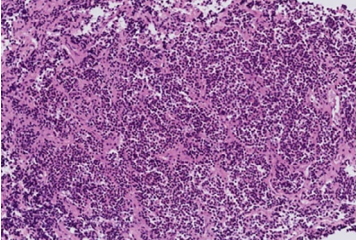
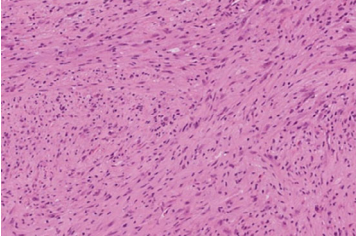
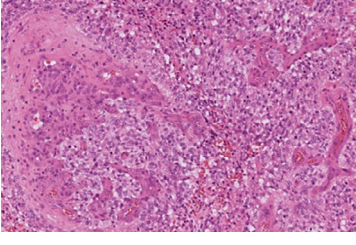
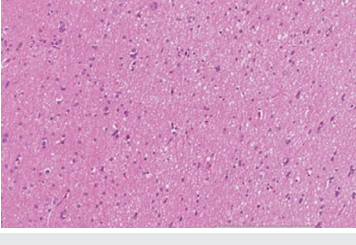
Tissue type	Nuclear density (nuclei/mm ²)
Tumour tissue	
Meningioma ($p = 3, n = 36$)	5245.85 (IQR: 3879.466407.36)
	
Pituitary adenoma ($p = 5, n = 48$)	8115.83 (IQR: 7203.218248.37)
	
Schwannoma ($p = 4, n = 36$)	Mean: 3930.65 (IQR: 2987.894967.87)
	
High grade glioma ($p = 2, n = 12$)	3660.71 (IQR: 2889.474257.74)
	
Low grade glioma ($p = 1, n = 6$)	808.88
	
Healthy cadaveric tissue	
Grey matter (frontal cortex)	803.76
White matter (frontal white matter)	1477.77
Grey and white matter (Pons)	451.96

TABLE 1 (Continued)

Tissue type	Nuclear density (nuclei/mm ²)
Cranial nerve (olfactory nerve)	1212.43
Cranial nerve (optic nerve)	735.20
Cranial nerve (occulomotor/trigeminal nerve)	1653.36
Anterior pituitary	4630.44
Pituitary stalk	3056.35
Dura	5736.00

Note: Tissue type: an illustrative H&E image of each tumour type is provided alongside the number of samples and measurements obtained (p , number of patients; n , number of spectrophotometer measurements). Nuclear density: Overall mean nuclear density values for each tissue type. Where applicable, additional nuclear density values are provided according to the tissue's morphological appearance.

spectrum of 400 to 1800 nm. We investigated the optical properties of meningioma, pituitary adenoma, schwannoma, low- and high-grade glioma and correlated these with the absorption and reduced scattering spectra of relevant anatomical tissues.

Measurements of absorption and reduced scattering spectra of human brain and tumour tissue have previously been acquired using spatially resolved diffuse reflectance measurements [25, 36] and frequency-domain photon migration [36] methods, whereas *ex vivo* measurements of freshly excised tissue have typically used an integrating sphere [25, 27, 37]. Others have also used an integrating sphere set-up to examine the optical properties of human brain and tumour tissue fixed in ethanol [38].

Ex vivo examination allows for more reproducible and more in-depth analysis of a tissue's optical properties across a wide wavelength range. Using a controlled experimental protocol, *ex vivo* analysis permits the detailed measurement of both reflectance and transmittance making the derivation of absorption and scattering coefficients over a wide spectral band more reliable. However, previous *ex vivo* studies have been significantly limited by the size of available samples. Standard port sizes on an integrating sphere typically measure 11 mm × 24 mm and 17 mm × 22 mm for transmittance and reflectance, respectively, but using our experimental setup it was possible to obtain reliable reflectance and transmittance measurements using a sample port size of 3 to 5 mm in diameter. It is worth noting that as discussed in Prah's IAD manual and in the study of Mesradi et al. [39], the distance (h) from the edge of the incident beam on the sample to the edge of the integrating sample port needs to be as large as practicable to ensure minimal light loss from the lateral sides of the sample. A failure to

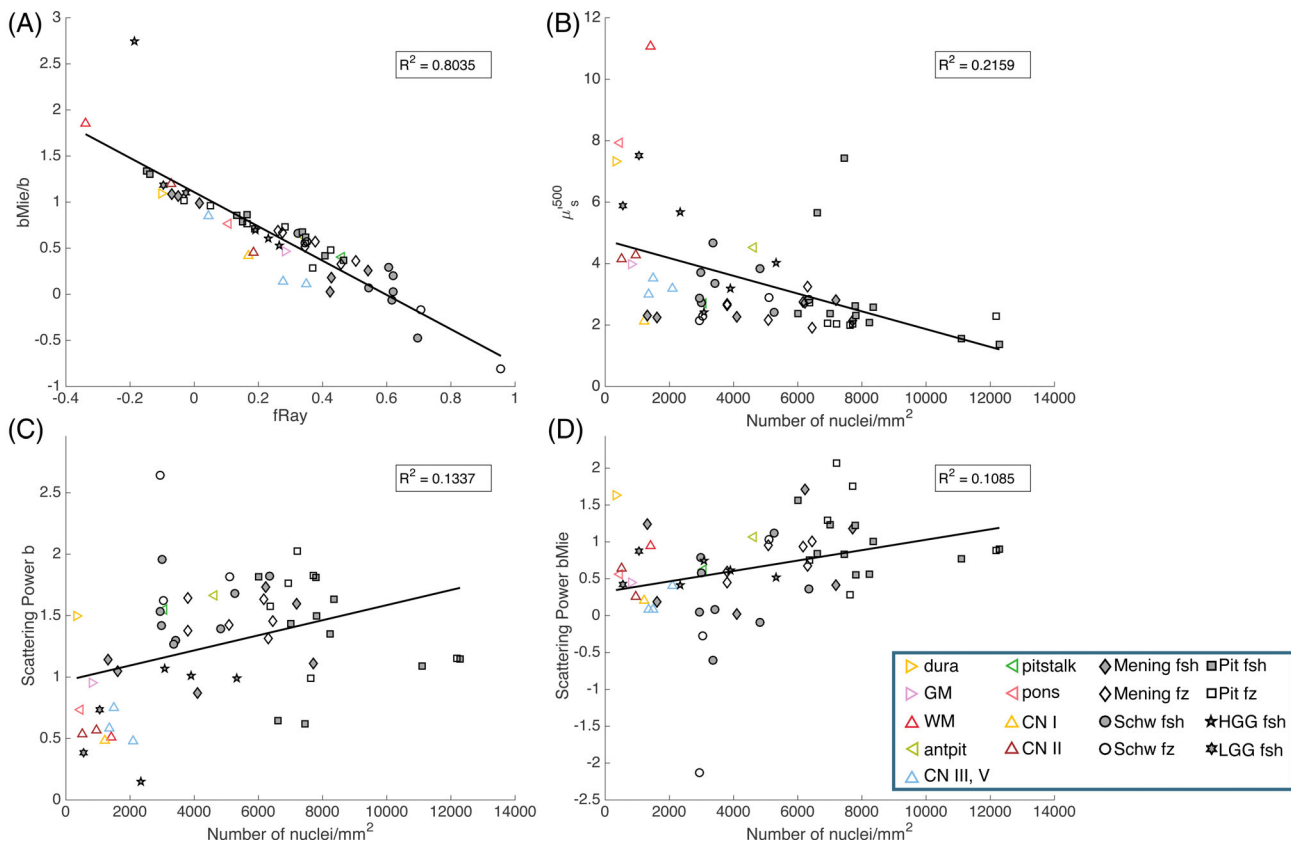


FIGURE 7 Tissues' constituent absorption and reduced scattering coefficients. Meningioma fsh: $p = 3$, $n = 18$; Schwannoma fsh: $p = 4$, $n = 24$; Pituitary adenoma fsh: $p = 5$, $n = 3$; Meningioma fz: $p = 3$, $n = 18$; Schwannoma fz: $p = 2$, $n = 12$; Pituitary adenoma fz: $p = 3$, $n = 18$; HGG fsh: $p = 2$, $n = 12$; LGG fsh: $p = 1$, $n = 6$; Post mortem samples (each) fz: $p = 1$, $N = 3$. (p : number of patients; n = number of spectrophotometer measurements). (A) Ratio of b_{Mie}/b and f_{Ray} . The fraction of b_{Mie}/b decreases with increasing f_{Ray} . (B–D): (B) Total absorption and nuclear density (nuclei/mm²); (C) Scattering power b and nuclear density (nuclei/mm²) and (D) Scattering power b_{Mie} and nuclear density (nuclei/mm²). (B–D) No evident correlation between the nuclei density and of the features of scattering (scattering power b , scattering power b_{Mie} , and μ'_s 500)

do so would lead to an overestimated absorption of the sample. In our study, the h value was 0.5 to 1.5 mm for the 3 mm port and 0.75 to 1.5 mm for the 5 mm port which satisfied the above constrain at most of the wavelength regions. However, we also noticed that a high $1/(\mu_a + \mu'_s)$ value, for example in the 700 to 1200 nm range, resulted in a strong light loss which meant that the IAD failed to converge. As described above in the methods section, individual single-wavelength measurements that did not converge were excluded.

By adapting our integrating sphere experimental setup, we were able to significantly expand the types of tissues that could be examined. Moreover, previous studies have only measured the optical properties of brain tissues at a limited number of wavelengths (Table S1). We used a standardized experimental setup to obtain the absorption and reduced scattering spectra of various human brain and tumour tissue at 10 nm increments across a wide wavelength spectrum of 400 to 1800 nm spanning the visible range to beyond the second near-

infrared window, thus providing a valuable reference tool (Table S1) for the development of future optical brain imaging technologies.

We observed that the spectral curves of every brain tumour had a similar shape to that of normal cadaveric human brain tissue (Figures 3–6). However, a tumour's reduced scattering coefficient ($\mu'_s{}^{fit}$) may be used to differentiate it from associated normal tissue (Figures 3–6; $\mu'_s{}^{fit}$). For example, for gliomas that typically arise within subcortical white matter, a difference was observed in the reduced scattering of glioma compared to white matter (Figure 6B). This could have significant implications for the design of diagnostic and therapeutic optical brain imaging devices. Similar to previous studies, the absorption spectra of all samples were dominated by the absorption bands of haemoglobin below 600 nm and water above 900 nm, with characteristic low absorption values within the 600 to 900 nm wavelength range [25, 27]. However, our results demonstrated a further striking peak in $\mu_a{}^{rev}$ at 1450 nm, not previously reported, but

consistent with the absorption spectra of water [40]. The reduced scattering coefficient spectra of all tissues generally decreased with increasing wavelength, while the values of reduced scattering were very different across all tissue types. Tissue absorption appeared to decrease with increasing nuclear density whereas a tissue's scattering power was positively associated with nuclear density but further work is required to determine the exact association between these variables.

The optical scattering of soft tissue is a result of the refractive index mismatch between lipid membranous structures and surrounding substances, and can be modelled as Mie scattering from spheres in the 0.2 to 2 μm diameter range [41]. In the shorter wavelength range (typically <500 nm), small-scale Rayleigh scatterers (size $\ll \lambda$) such as membranes of lipid and protein (0.1–0.2 μm thickness), are attributed to the rapid drop of reduced scattering as wavelength increases. This is particularly apparent in tumour tissue, grey matter and white matter (Figure 7A). In the longer wavelength (>500 nm) large-scale Mie scatterers (size $\geq \lambda$), such as cell nuclei (5–10 μm in diameter) and mitochondria (1–2 μm in diameter) are dominating [41, 42]. As expected, our results demonstrated that densely cellular high grade glioma tissue had similar scattering properties to grey matter which consists primarily of neuronal cell bodies (Figures 3D and 6B). However, gliomas typically arise from within white matter. Given that other internal cytoplasmic structures contribute a significant portion of a tissue's scattering properties [43] it would be interesting for further study to investigate the relative contribution of tumoural vascular and collagen fibre density.

As noted in previous studies [25, 27], we also observed inter-parameter crosstalk between the tissue's relative absorption and reduced scattering coefficients in wavelengths. In wavelength regions associated with chromophore absorption peaks, the revised absorption coefficient has a higher value than the originally calculated μ_a^{IAD} ; presumably because the crosstalk created local maxima in the scattering spectra is compromised/smoothed out with the μ_s^{fit} value (Figures 3 and 4 [Figures S3 and S4]). Given that the highest absorption peak of water occurred at 1450 nm, it was not surprising that the highest degree of crosstalk also occurred at this wavelength.

This phenomenon was most pronounced in cortical grey matter and pons tissue but was also seen in healthy dura and pituitary tissue and to a lesser degree in the tumour samples. This may be explained by the fact that those tissues exhibiting this phenomenon are predominantly composed of cell bodies whereas white matter consists predominantly of myelinated axons. To mitigate for the crosstalk effect, we developed a two-stage IAD

method to revise the μ_a by using fitted μ_s as input constrain of IAD (Figures 3–6). It could be further improved by using Equation (1) fitted μ_s' including a separately fitted short wavelength region (Rayleigh limit) and longer wavelength region in order to address the crosstalk created by haemoglobin and water, respectively. It was also noticeable that some reduced scattering coefficient results were associated with a rather large SD, particularly fresh pituitary adenoma (Figure 4B) and HGG (Figure 6B). Previous publications opted to present their data using the mean and Standard Error of the Mean (SEM) and consequently presented results with seemingly much smaller error bars [25, 27]. Similar SEM were obtained with our data (Table S1) but we felt that displaying the SD reflected the inherent variability within tissue types more effectively.

We investigated what effect the freezing process might have on the tissues' optical properties using tumour samples. Roggan et al. and Mesradi et al. previously observed that snap-freezing porcine and rat tissue produced significant changes in the tissues' absorption and reduced scattering coefficients [39, 44]. However, following a quick comparison study, Gebhart et al. brief concluded that “snap freezing, tissue storage and thawing in saline had minimal effect on the measurement absorption and reduced scattering coefficients” [25]. In our study, a systematic comparison of the optical properties of two fresh and two frozen tumour samples taken from each specimen suggested that the freezing process did affect the sample's absorption coefficient, particularly within the wavelength range of 700 to 1100 nm (Figures 3–5).

Various methods have been developed and applied to determine the optical properties of brain tissue, including different combinations of experimental methods for obtaining measurements, and different numerical algorithms to calculate the optical properties from the measurements. There is a great variability in the determined optical properties in different studies mainly due to the theories that have been employed and possible tissue preparation artefacts [26, 45]. In this study, we compared our findings of the calculated absorption coefficient and reduced scattering coefficient of various brain and tumour tissues to the works of Bevilacqua et al. [36], Gebhart et al. [25] and Yaroslavsky et al. [27] as illustrated in Figure 8 and tabulated in Table S1. The study's complete numerical dataset is published as part of the study's supplementary material and may be re-used by the research community. Despite the differences in tissue preparation and calculation methods, the absorption values from our study were consistent with other studies in all available tissue types (Figure 8A–F). However, a surprising and persistent offset in the magnitude of the

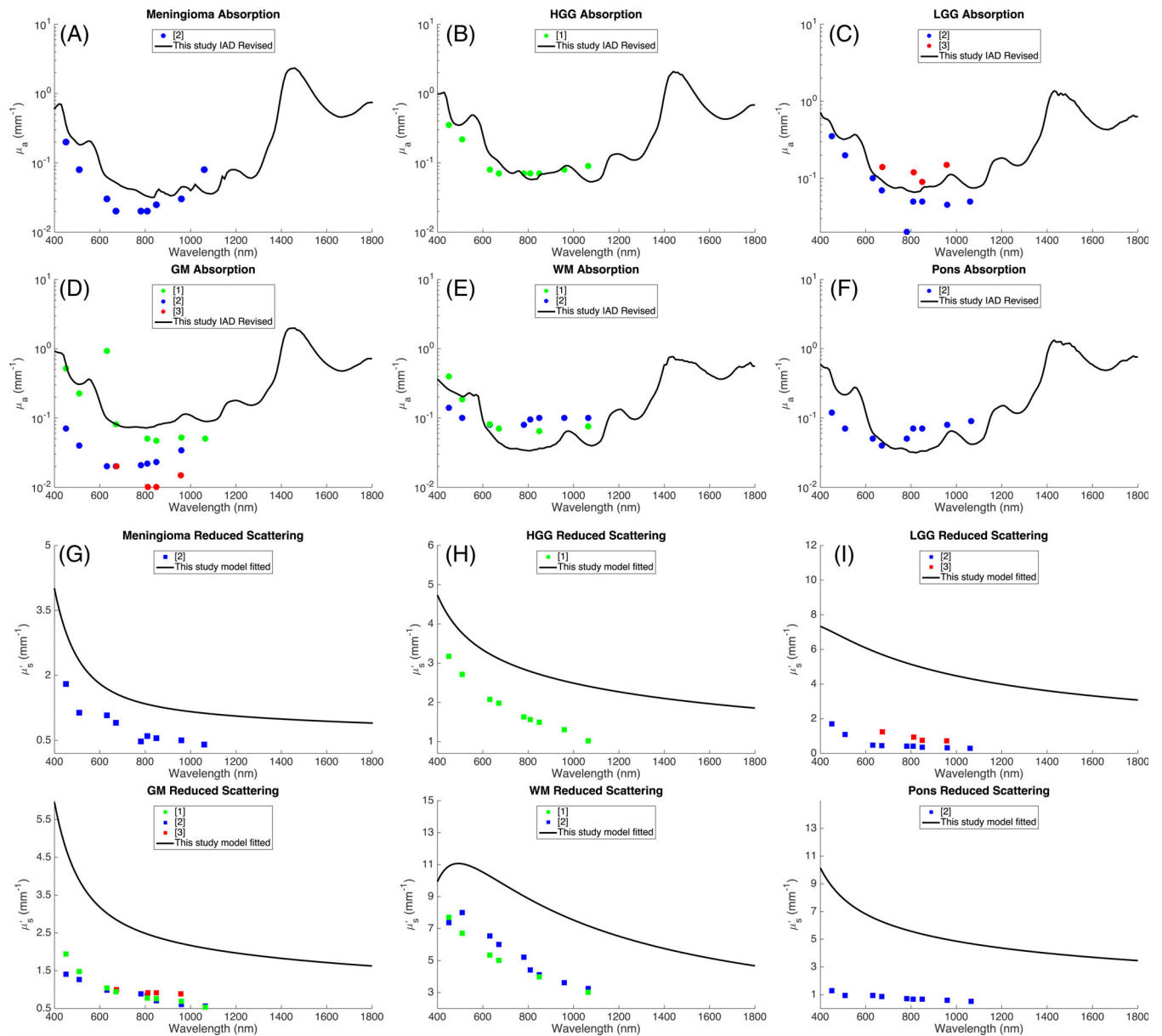


FIGURE 8 Absorption and reduced scattering coefficient of brain and tumour tissue: a comparison with previous results.

(A) Absorption of meningioma, (B) high grade glioma (HGG), (C) low grade glioma (LGG), (D) grey matter (GM), (E) white matter (WM) and (F) Pons. (G) Reduced scattering of meningioma, (H) high grade glioma (HGG), (I) low grade glioma (LGG), (J) grey matter (GM), (K) white matter (WM) and (L) Pons. Additional values were estimated from the graphical plots included in the published manuscripts. All data available in Table S1

reduced scattering was observed in all tissue types (Figure 8G–L). The mean value of the derived model fitting parameters b and b_{Mie} averaged from brain tissues in this study were 1.30 and 0.58, respectively, which are comparable to the values presented in the review work of Jacques ($b = 1.611$, $b_{\text{Mie}} = 0.315$) [23].

We examined both fresh and frozen brain tumour tissue as well as frozen healthy brain tissue obtained post-mortem. In previous *ex vivo* studies using an integrating sphere, studies analysed thawed frozen tissue [25, 27]. In our study, we analysed freshly excised tumour tissue

within 30 min of removal. Some cellular change may have occurred in the tissue during this interval but by minimising the time from resection to analysis, we aimed to obtain results that most closely resembled *in vivo* measurements. Frozen tumour samples were also prepared and stored within 30 min of removal. It was not feasible for us to obtain freshly excised normal brain tissue, hence we examined samples obtained postmortem. In this case, the subject had died 6 days prior to their postmortem examination which may have also induced some discrepancies in results.

A recognized limitation in the optical analysis of ex vivo tissue is that the process of tissue excision may produce changes in its optical properties in particular due to blood drainage; however, these effects are predictable as a loss of absorption coefficient [46]. Despite these changes, it has been shown that the differential path-length of light in tissue measured post mortem is similar to that measured in vivo [47]. Nevertheless, the analysis of ex vivo and post mortem tissue will never be able to take into account in vivo variations in blood flow and haemoglobin oxygenation saturation and these will inherently undergo some change with time and the method of tissue storage and transportation. We also observed that a small number of samples demonstrated cellular autolysis by the time histological analysis was performed. The presence of cellular autolysis was not reflective of the state of the tissue during optical evaluation, rather the delay between optical and histological review. Other limitations of this study include the small number of subjects and the spread within numerical estimations. Companion methodological work is currently underway to validate the model fitting described in this study beyond the simulation study presented here.

This study provides a comprehensive evaluation of the optical properties of various human brain tumour and healthy brain tissues. Detailed knowledge of a tissue's optical properties will greatly assist in the development of modern intraoperative optical imaging methods and could therefore facilitate the delivery of computational image analysis during surgery. For example, this dataset may be used as ground truth data to model different intraoperative surgical scenarios to train, test and validate new optically based machine learning classifiers.

Comparison data from:

1. Gebhart et al., [25]: Grey matter, white matter and glioma. Reported wavelengths: 450, 510, 630, 670, 850 and 1064 nm. Values calculated using Inverse Adding Doubling (IAD) method.
2. Yaroslavsky et al., [27]: Grey matter and white matter. Meningioma, astrocytoma (WHO grade II) and pons also measured but specific values not reported. Reported wavelengths: 450, 510, 630, 670, 850, 956 and 1064 nm. Values calculated using Inverse Monte Carlo (IMC) method.
3. Bevilacqua et al., [36]: Normal frontal cortex, normal optic nerve and optic nerve astrocytoma (presumed pilocytic astrocytoma, WHO grade I but not specified). Optic nerve astrocytoma compared with parenchymal LGG measurements. Reported wavelengths: 674, 811,

849 and 956 nm. Values calculated using Inverse Monte Carlo (IMC) method.

5 | CONCLUSION

We investigated the ex vivo optical properties of five types of human brain tumour and nine different types of healthy brain tissue across a wavelength spectrum of 400 to 1800 nm spanning the visible range to beyond the second near-infrared window. All tissue types demonstrated similar absorption spectra but the reduced scattering coefficients of tumours were clearly different to those of surrounding normal tissue. These results have significant potential for the development of intraoperative optical imaging technologies.

ACKNOWLEDGMENTS

This study was supported by Wellcome Trust [203145Z/16/Z; 203148/Z/16/Z; WT106882], EPSRC [NS/A000050/1; NS/A000049/1] and National Brain Appeal [NBA/T&I/N-ONC] funding. Tom Vercauteren is supported by a Medtronic/Royal Academy of Engineering Research Chair [RCSR1819\7\34].

DATA AVAILABILITY STATEMENT

The data that supports the findings of this study are available in the supplementary material of this article.

ORCID

Jonathan Shapey  <https://orcid.org/0000-0003-0291-348X>

Yijing Xie  <https://orcid.org/0000-0002-3432-8587>

REFERENCES

- [1] A. M. Zysk, F. T. Nguyen, A. L. Oldenburg, D. L. Marks, S. A. Boppart, *J. Biomed. Opt.* **2007**, *12*(5), 051403.
- [2] L. M. Sakata, J. DeLeon-Ortega, V. Sakata, C. A. Girkin, *Clin Exp Ophthalmol* **2009**, *37*(1), 90.
- [3] H. G. Bezerra, M. A. Costa, G. Guagliumi, A. M. Rollins, D. I. Simon, *JACC: Cardiovasc Interv* **2009**, *2*(11), 1035.
- [4] E. Sattler, R. Kästle, J. Welzel, *J. Biomed. Opt.* **2013**, *18*(6), 061224.
- [5] T. Nagaya, Y. A. Nakamura, P. L. Choyke, H. Kobayashi, *Front Oncol* **2017**, *7*, 314.
- [6] Q. T. Nguyen, R. Y. Tsien, *Nat Rev Cancer* **2013**, *13*(9), 653.
- [7] W. Stummer, U. Pichlmeier, T. Meinel, O. D. Wiestler, F. Zanella, H. J. Reulen, *Lancet Oncol.* **2006**, *7*(5), 392.
- [8] J. Desroches, M. Jermyn, M. Pinto, F. Picot, M. A. Tremblay, S. Obaid, E. Marple, K. Urmey, D. Trudel, G. Soulez, M. C. Guiot, B. C. Wilson, K. Petrecca, F. Leblond, *Sci. Rep.* **2018**, *8*(1), 1792.
- [9] M. Jermyn, K. Mok, J. Mercier, J. Desroches, J. Pichette, K. Saint-Arnaud, L. Bernstein, M. C. Guiot, K. Petrecca, F. Leblond, *Sci. Transl. Med* **2015**, *7*(274), 274ra19.

- [10] M. Jermyn, J. Desroches, K. Aubertin, K. St-Arnaud, W. J. Madore, E. De Montigny, M. C. Guiot, D. Trudel, B. C. Wilson, K. Petrecca, F. Leblond, *Phys. Med. Biol.* **2016**, *61*(23), R370.
- [11] P. Campagnola, *Anal. Chem.* **2011**, *83*(9), 3224.
- [12] S. A. Toms, W.-C. Lin, R. J. Weil, M. D. Johnson, E. D. Jansen, A. Mahadevan-Jansen, *Oper. Neurosurg* **2005**, *57*(suppl_4), 382.
- [13] P. V. Butte, Q. Fang, J. A. Jo, W. H. Yong, B. K. Pikul, K. L. Black, L. Marcu, *J. Biomed. Opt.* **2010**, *15*(2), 27008.
- [14] Y. H. Sun, N. Hatami, M. Yee, et al., *J. Biomed. Opt.* **2010**, *15*(5), 56022.
- [15] S. D. Konecky, C. M. Owen, T. Rice, P. A. Valdés, K. Kolste, B. C. Wilson, F. Leblond, D. W. Roberts, K. D. Paulsen, B. J. Tromberg, *J. Biomed. Opt.* **2012**, *17*(5), 56008.
- [16] M. Sibai, D. J. Wirth, F. Leblond, D. W. Roberts, K. D. Paulsen, B. C. Wilson, *J. Biophotonics* **2019**, *12*(5), e201800271.
- [17] P. Beard, *INTERFACE Focus* **2011**, *1*(4), 602.
- [18] J. Shapey, Y. Xie, E. Nabavi, R. Bradford, S. R. Saeed, S. Ourselin, T. Vercauteren, *J. Biophotonics* **2019**, *12*, e201800455.
- [19] N. T. Clancy, G. Jones, L. Maier-Hein, D. S. Elson, D. Stoyanov, *Med. Image Anal.* **2020**, *63*, 101699.
- [20] J. R. Mourant, J. P. Freyer, A. H. Hielscher, A. A. Eick, D. Shen, T. M. Johnson, *Appl Opt* **1998**, *37*(16), 3586.
- [21] B. Costas, P. Christos, E. George, Multi/hyperspectral imaging. in *Handbook of Biomedical Optics* (Eds: D. A. Boas, C. Pitris, N. Ramanujam), CRC Press, Boca Raton, FL **2011**, p. 131.
- [22] F. Huth, A. Govyadinov, S. Amarie, W. Nuansing, F. Keilmann, R. Hillenbrand, *Nano Lett.* **2012**, *12*(8), 3973.
- [23] S. L. Jacques, *Phys Med Biol* **2013**, *58*(11), 5007.
- [24] J. W. Pickering, S. A. Prahl, N. van Wieringen, J. F. Beek, H. J. C. M. Sterenborg, M. J. C. van Gemert, *Appl. Opt.* **1993**, *32*(4), 399.
- [25] S. C. Gebhart, W. C. Lin, A. Mahadevan-Jansen, *Phys. Med. Biol.* **2006**, *51*(8), 2011.
- [26] S. Madsen, B. Wilson, *Optical Properties of Brain Tissue*, Vol. 3, Springer, New York **2013**.
- [27] A. N. Yaroslavsky, P. C. Schulze, I. V. Yaroslavsky, R. Schober, F. Ulrich, H. J. Schwarzmaier, *Phys. Med. Biol.* **2002**, *47*(12), 2059.
- [28] Y. Xie, J. Shapey, E. Nabavi, et al., *arXiv* **2021**.
- [29] J. Shapey, Y. Xie, E. Nabavi, et al., *Label-free Biomed. Imaging Sens* **2020**, *11251*, 112510J.
- [30] P. Bankhead, M. B. Loughrey, J. A. Fernández, Y. Dombrowski, D. G. McArt, P. D. Dunne, S. McQuaid, R. T. Gray, L. J. Murray, H. G. Coleman, J. A. James, M. Salto-Tellez, P. W. Hamilton, *Sci. Rep.* **2017**, *7*(1), 16878.
- [31] S. A. Prahl, M. J. van Gemert, A. J. Welch, *Appl Opt* **1993**, *32*(4), 559.
- [32] J. M. Schmitt, G. Kumar, *Opt. Lett.* **1996**, *21*(16), 1310.
- [33] S. Golovynskiy, I. Golovynska, L. I. Stepanova, O. I. Datsenko, L. Liu, J. Qu, T. Y. Ohulchanskyy, *J. Biophotonics* **2018**, *11*(12), e201800141.
- [34] S. L. Jacques, *Generic Tissue Optical Properties*, Medical Laser Centre, Oregon **2015**.
- [35] S. Prahl, "Optical Absorption of Hemoglobin," **1999**. <http://omlc.ogi.edu/spectra/hemoglobin>
- [36] F. D. R. Bevilacqua, D. Pigué, P. Marquet, J. D. Gross, B. J. Tromberg, C. Depeursinge, *Appl. Opt.* **1999**, *38*(22), 4939.
- [37] J. F. Beek, P. Blokland, P. Posthumus, M. Aalders, J. W. Pickering, H. J. C. M. Sterenborg, M. J. C. van Gemert, *Phys. Med. Biol.* **1997**, *42*(11), 2255.
- [38] F. Poulon, H. Mehidine, M. Juchaux, P. Varlet, B. Devaux, J. Pallud, D. Abi Haidar, *Sci. Rep.* **2017**, *7*(1), 13995.
- [39] M. Mesradi, A. Genoux, V. Cuplov, D. Abi Haidar, S. Jan, I. Buvat, F. Pain, *J. Biomed. Opt.* **2013**, *18*(11), 117010.
- [40] V. Nguyen, Y. Paulus, V. P. Nguyen, Y. M. Paulus, *J. Imaging* **2018**, *4*(12), 149.
- [41] S. L. Jacques, *OSA TOPS Adv. Opt. imaging Phot. Migr.* **1996**, *2*, 364.
- [42] V. V. Tuchin, Tissue optics. in *Society of Photo-Optical Instrumentation Engineers (SPIE)*, SPIE, Bellingham, WA **2015**.
- [43] J. R. Mourant, M. Canpolat, C. Brocker, O. Esponda-Ramos, T. M. Johnson, A. Matanock, K. Stetter, J. P. Freyer, *J. Biomed. Opt.* **2000**, *5*(2), 131.
- [44] A. Roggan, D. Schädel, U. Netz, J. P. Ritz, C. T. Germer, and G. Müller, "," *Appl. Phys. B Lasers Opt.*, vol. 69, no. 5, pp. 445–453, Nov. **1999**.
- [45] V. Tuchin, Polarization-sensitive techniques. in *Tissue Optics*, SPIE, Bellingham, WA **2010**, p. 489.
- [46] C. R. Simpson, M. Kohl, M. Essenpreis, M. Cope, *Phys. Med. Biol.* **1998**, *43*(9), 2465.
- [47] D. T. Delpy, M. Cope, P. van der Zee, S. Arridge, S. Wray, J. Wyatt, *Phys. Med. Biol.* **1988**, *33*(12), 1433.

SUPPORTING INFORMATION

Additional supporting information may be found in the online version of the article at the publisher's website.

How to cite this article: J. Shapey, Y. Xie, E. Nabavi, M. Ebner, S. R. Saeed, N. Kitchen, N. Dorward, J. Grieve, A. W. McEvoy, A. Misericchi, P. Grover, R. Bradford, Y.-M. Lim, S. Ourselin, S. Brandner, Z. Jaunmuktane, T. Vercauteren, *J. Biophotonics* **2022**, *15*(4), e202100072. <https://doi.org/10.1002/jbio.202100072>